ARTICLE

Segmental and interfacial dynamics quantitatively determine ion transport in solid polymer composite electrolytes

Yage Huang | Xintong Mei | Yunlong Guo

University of Michigan – Shanghai Jiao Tong University Joint Institute, Shanghai Jiao Tong University, Shanghai, China

Correspondence
Yunlong Guo, University of Michigan – Shanghai Jiao Tong University Joint Institute, Shanghai Jiao Tong University, Shanghai 200240, China.
Email: yunlong.guo@sjtu.edu.cn

Abstract

Solid polymer-ceramic composite electrolytes (PCEs) have attracted vast attention for developing solid-state batteries. However, slow ion transport at ambient temperature impedes unlocking their potential. Improving ionic conductivity of PCEs remains a major challenge, because ion transport mechanism in complicated composites is not currently available. This article, for the first time, demonstrates that segmental motion and interfacial polarization are directly coupled, both quantitatively determine ion transport in PCEs. Adding small-molecule additives enhances ionic conductivity in PCEs, by increasing concentration of ions participating in transport and by equally accelerating segmental motion and interfacial dynamics. Accordingly, an ionic conductivity achieves 1.3×10^{-3} S/cm at 30°C, simultaneously with high mechanical strength and toughness (solid and flexible, shear modulus $G' > 1$ MPa). The results may shed a light for better analysis and improved design of solid composite electrolytes, toward meeting material demands for next-generation electrochemical energy storage.

KEYWORDS
ion transport, interfacial polarization, polymer-ceramic composite electrolytes, segmental dynamics, solid state battery

1 | INTRODUCTION

The development of solid-state electrolytes (SSEs) is crucial to meet the challenge of material demands in next-generation secondary batteries where electrodes and electrolytes are widely recognized to be solid materials.[1] To achieve an exceptional electrochemical performance, structural stability, and battery safety, typical cutting-edge SSEs integrate merits from multiple materials, including fast ion transport in ceramics and mechanical flexibility in polymers.[2] Consequently, polymer–ceramic composite electrolytes (PCEs) attract tremendous scientific and technological interest.[3–7] For instance, a great deal of attention has been paid to composites fabricated by dispersing garnet-type

particles in poly(ethylene oxide) (PEO) host, while keeping their traits of low cost and suitable mechanical toughness.[8] Despite recent progress in such PCEs, their low ionic conductivity (~10^{-4} S/cm) at ambient temperature remains a formidable obstacle.

Mechanisms of ion transfer in solid composites are complicated. Microstructures and phases, together with physical and chemical properties of various constituents significantly affect ionic conductivity and ion-transport pathways. In a polymer matrix, ionic motion is strongly coupled with segmental dynamics of the chain molecules.[9–11] Ion transport is contributed from both sub-diffusive motion along chain segments and inter-segmental hopping.[12] To achieve a competitive ionic

conductivity, addition of ceramic particles benefits polymer electrolytes by reducing crystallinity, although the original intention for introducing such fillers is to exploit their superiority in ion transport. It has been demonstrated that small particles with relatively low fractions enhance ion transport, which is in line with percolation simulations.[13,14] Nevertheless, insufficient loading often makes limited continuous pathways along interconnected ceramic particles, whereas overabundant fillers usually agglomerate and result in loss of interphase volume hence obstructing formation of percolating network, known as the blocking effect.[15] Ion transport through polymer domain is indispensable under such scenario.

Following the strategy of building continuous freeway for Li$^+$, recent works using oriented nanowires showed a considerable increase of ionic conductivity, and exhibited ion pathways on the surface of nanowires.[16–18] Moreover, the preference of ion transport along interface rather than entering interior of ceramics, was further proved by the high conductivity under large volume fraction of interfaces.[19] In addition, new twists ranging from copolymerization,[20–22] chain network,[23,24] polymer blend,[25] and nano-porous structure,[19,26] to ionic side group[27] and plasticizer,[28,29] bring promising improvements. Releasing the potential of solid composite electrolytes requires mastering mechanism of ion transport in such materials. However, in multiphase PCEs, models quantitatively demonstrating ion transport through polymer domains and surface charge layers are still unavailable.

This study establishes quantitative coupling equations, for the first time, between ion transport and multiple micro-dynamic processes in PCEs, that is, the electrochemical impedance spectrum (EIS) properties can be fully described and predicted by dielectric relaxation spectroscopy (DRS) dynamic analysis. Li$^+$ transfer rate strongly depends on relaxation time and dielectric strength in polymer chains and at polymer-ceramic interfaces. Adding plasticizer raises ionic conductivity ($>10^{-3}$ S/cm at 30°C) by equally accelerating segmental and interfacial dynamic processes. With this information, the ion transfer mechanism is deeply understood, which offers valuable strategies for increasing ambient σ_{dc} in PCEs.

Our samples consist of Li$_{6.4}$La$_3$Zr$_{1.4}$Ta$_{0.6}$O$_{12}$ (LLZTO) or SiO$_2$ particles, uniformly dispersed in PEO host, with various weight loadings. LiClO$_4$ salt is added to the composite with a molar ratio to EO of 1:18. The samples are accordingly labeled by PEO$_{18}$-LiClO$_4$-x wt% LLZTO (or SiO$_2$) where the labels indicate the particle diameter. In other cases, certain amount of plasticizer diethylene glycol dimethyl ether (DEGDME) was introduced into the sample, to probe the origin of ion transport enhancement by tuning micro-dynamics.

2 | RESULTS AND DISCUSSION

2.1 | Correlation between local dynamics and electrochemical impedance response

Figure 1 correlates the microscopic dynamic processes with the electrochemical property in a representative PCE. The frequency spectra of dielectric permittivity (Figure 1a) can be divided into three regions, which are dominated by segmental relaxation (α and α_2 process), Maxwell–Wagner–Sillars (MWS) interfacial polarization, and electrode polarization (EP), respectively. Boundaries of these regions are determined from the second-order derivative of ε'_r, as interpreted in Appendix. At 10^3–10^4 Hz, a frequency zone led by the α_2 relaxation and MWS process, ε''_r shows a linear dependence with a rate of -0.94 (inset in Figure 1a), indicating the ionic transport. Correspondingly, the ionic conductivity (σ_{dc}) is determined from in-phase part of $\sigma'(\omega) = \varepsilon''_r(\omega)\varepsilon_0\omega$, where ε_0 is the permittivity of vacuum. The permittivity response is decomposed into several key contributors, as demonstrated in Figure 1b. From the trend of gradual leveling off of ε''_r at high frequencies, we detected two α processes, which are speculated to be originated from the relative fast (α) and slow (α_2) modes of segmental motion under different levels of confinement of amorphous phases among LLZTO particles and PEO crystal phases.

Remarkably, intensities of dynamic processes show an inverse relationship with the frequency. This trend reflects the large length scale and greater number of ions getting involved in the individual dynamic processes from segmental motion, to MWS polarization, and to EP.

To examine the influence of segmental relaxation and interfacial polarization on ionic conductivity in solid PCEs, EIS was measured with two stainless steel blocking electrodes for various samples. In line with the permittivity results, EIS exhibits three major regions with approximately identical boundaries, as marked in Figure 1c. From high to low frequencies, the regions show a semicircle, a slightly curved line, and a spike, respectively, representing the responses from local dynamics in amorphous phase of PEO, PEO-LLZTO dielectric boundary layers, and electrolyte-electrode interfaces. This is further confirmed by reproducing the EIS profile using Nyquist characteristics of segmental relaxations, MWS polarization, and EP.[30] The dash curves in Figure 1c,d are computed from the results in Figure 1b according to $\varepsilon_r \times (\omega) = 1/(i\omega Z \times (\omega)C_0\varepsilon_0)$, where C_0 is the capacitance of the empty capacitor. The sum of impedance from these dynamic processes (black curve, slightly smoothed) matches the data well. These results suggest a direct and strong correlation between micro-dynamics and EIS results exists. That is, the electrochemical response can
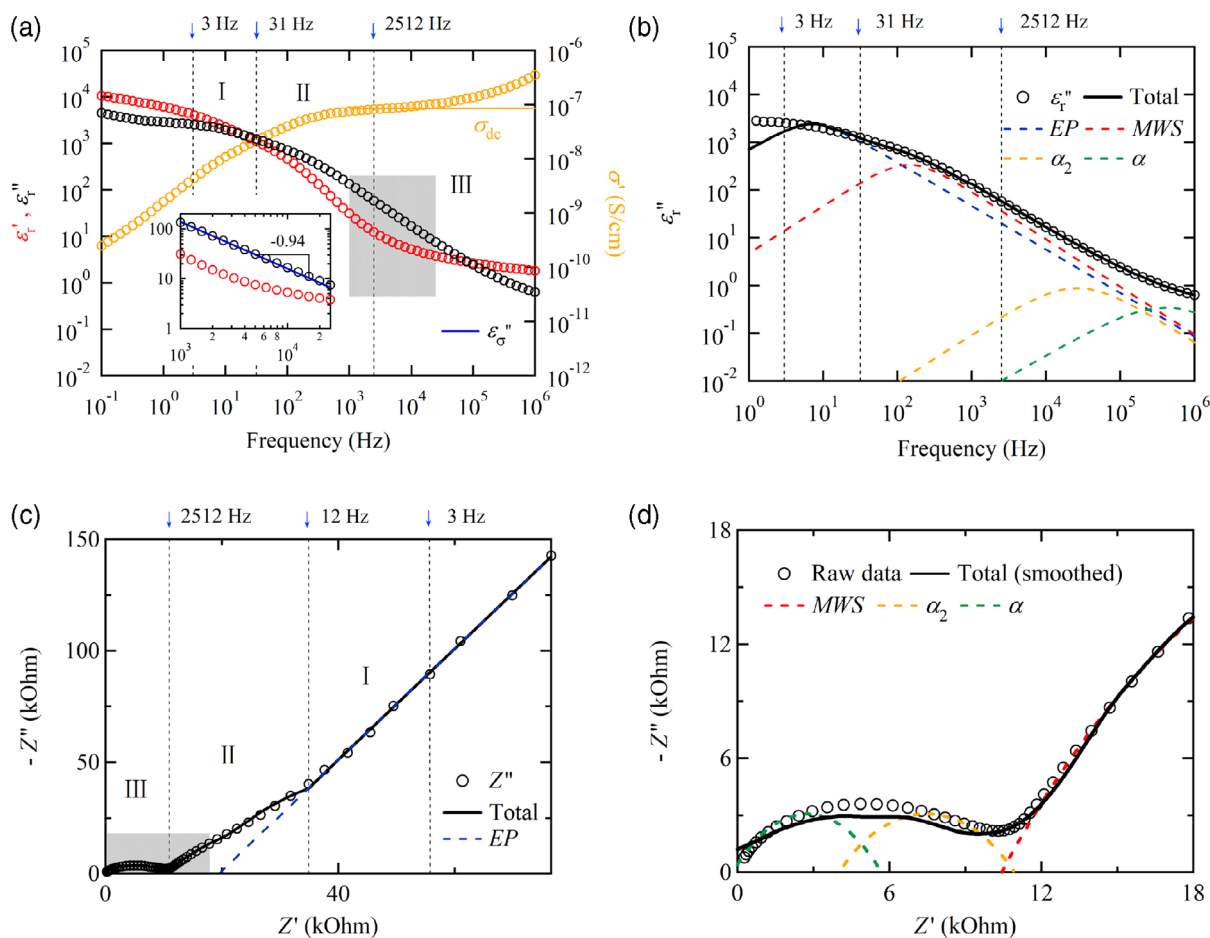
FIGURE 1 Representative dielectric frequency spectra and Nyquist plot of ac-impedance measurements. (a) Dielectric relaxation spectra. The inset shows an ionic conduction with a slope of nearly -1 in the gray area. (b) Decomposition of the loss dielectric permittivity into several sub-processes. The dash curves represent processes described by Equations (7) and (8). (c) The corresponding Nyquist plot under identical condition. Open circles represent raw data from electrochemical impedance spectrum measurements, while the solid curve represents the sum of response from dynamic processes. (d) Details of the gray area in (c). I, II, and III in (a) and (c) represent regions dominated by electrode polarization, Maxwell–Wagner–Sillars and segmental relaxations, respectively. Data are measured at 10°C, for the sample of PEO_{18}-$LiClO_4$ with dispersed 100 nm-SiO_2 particles at 10 wt% [Color figure can be viewed at wileyonlinelibrary.com]

be derived from, and controlled by dynamic processes in which ion transport gets involved, without conducting EIS measurements.

2.2 | Modeling ionic conductivity

EIS measurements were conducted on our PCE samples containing inert (SiO_2) or superior ion conductor (LLZTO) particles at various temperatures. Selected PCEs with DEGDME additives, as model materials to investigate mechanism of σ_{dc} enhancement, were tested as well. The highest σ_{dc} at 30°C detected in our testing is 1.3×10^{-3} S/cm in PEO_{18}-$LiClO_4$-10 wt% 500 nm-LLZTO-5 wt% DEGDME. It also exhibits good toughness (integrality and flexibility) and mechanical strength[11,31]

($G' > 1$ MPa at 30°C), as shown in Figure 2c,d. The membrane is in solid-state, confirmed by $G' > G''$. With further increase of DEGDME content as depicted in Figure 2a, the σ_{dc} monotonically reduces. This trend qualitatively matches simulation results by the percolation theory.[15] The enlarged space of σ_{dc} alteration, depending on several control parameters, provides a foundation for analyzing mechanism of ion transport in PCEs.

To demonstrate the governing equations of ionic conductivity using parameters of dynamic relaxations, we further explore correlations between σ_{dc} and relaxation time (τ_{inter}, τ_α) or dielectric strength ($\Delta\varepsilon_{inter}$, $\Delta\varepsilon_\alpha$). Considering the fillers and the surrounding surface charge layer as two in-series layers, the characteristic time of MWS polarization is given by[32]:
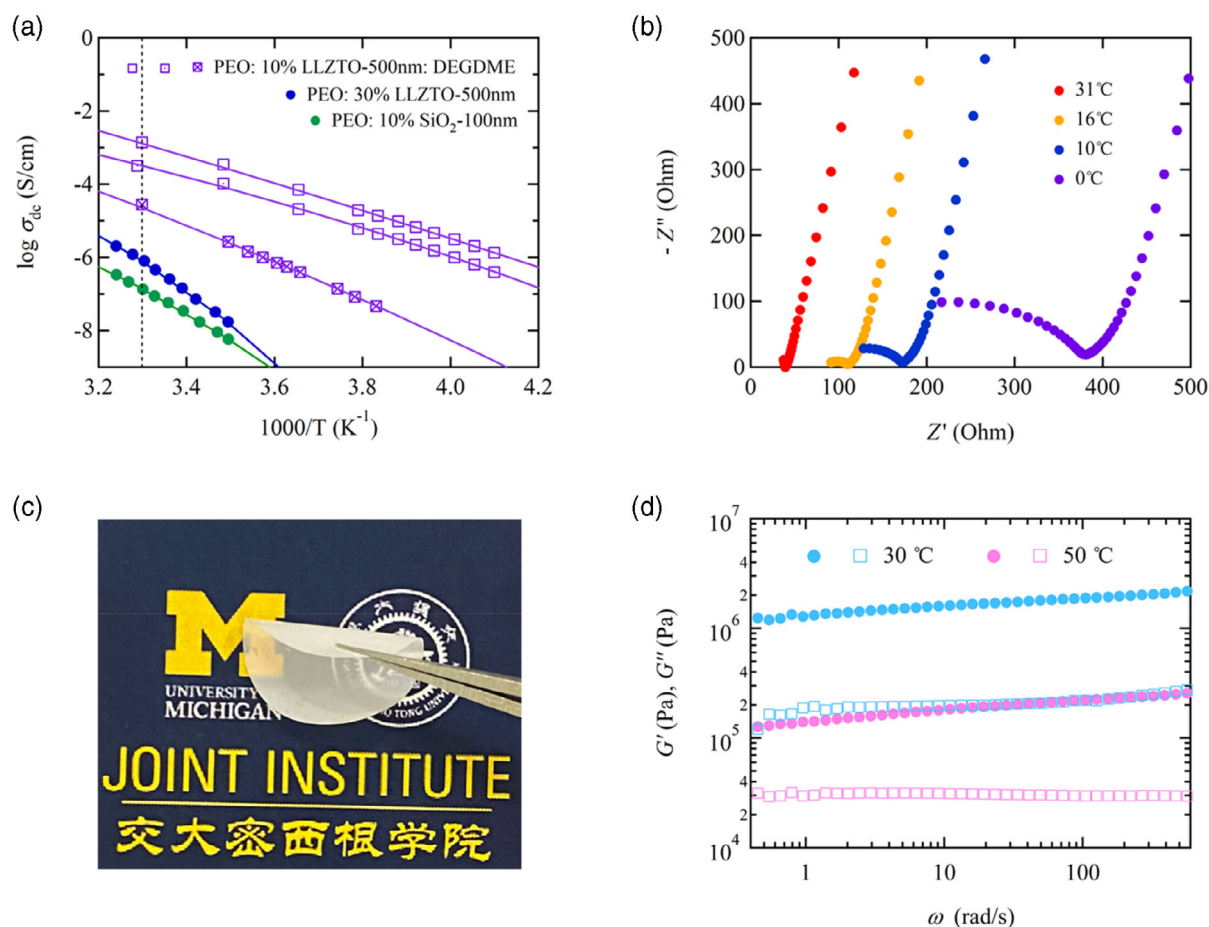
FIGURE 2 Ionic transport in selected samples. (a) Representative dc conductivity as a function of inverse temperature. Dash line indicates 30°C. Symbols of □, ⊡ and ⊠ represent data from samples with increasing weight fraction of DEGDME. (b) Nyquist plots at various temperatures. (c) Photograph of a freestanding membrane shows flexibility. Sample: PEO_{18}-$LiClO_4$-10 wt% 500 nm-LLZTO-5 wt% DEGDME. (d) Shear modulus as a function of frequency of the sample in (c) at 30 and 50°C. Filled circles and open squares represent the storage modulus G' and loss modulus G'', respectively [Color figure can be viewed at wileyonlinelibrary.com]

$$\tau_{inter} \approx \tau_c \delta = \frac{\varepsilon_0 \varepsilon_s}{\sigma_{dc}} \delta, \qquad (1)$$

and

$$\delta = \frac{D_v}{2L_D} = \frac{\varepsilon_s}{\varepsilon_\infty}, \qquad (2)$$

where τ_c is the mean relaxation time for conductivity, D_v is the average diameter of particles, in this work obtained from 3D nano CT imaging (Figures S2–S4), L_D is the Debye length.

Combing Equation (1) and (2), we get

$$\log(\sigma_{dc}) = -\log(\tau_{inter}) + \log\left(\frac{\varepsilon_0 \varepsilon_s^2}{\varepsilon_\infty}\right). \qquad (3)$$

In a similar form, σ_{dc} correlates with the α (or α_2) process[33]:

$$\log(\sigma_{dc}) = -\log(\tau_\alpha) + C, \qquad (4)$$

where C is a constant. Thus $1/\tau_\alpha$ can be considered as a measure of the velocity of ion dissociation. Figure 3 summarizes the influence of MWS and α relaxation on σ_{dc}. Equation (3) quantitatively describes the effect of τ_{inter} in most samples (Figure 3a), except for the data set of PEO_{18}-$LiClO_4$-5 μm-SiO_2 at low weight loadings. Similar trend is also found after adding of DEGDME (Figure S18). In these cases, τ_c values may show a distribution across the interface leading to a more complicated situation,[34] and hence τ_{inter} is no longer being proportional to τ_c. As shown in Figure 3a,b, plasticizer increases σ_{dc} by accelerating interfacial and segmental dynamics, leading to a reduction of τ_{inter} and τ_α. In contrast, ceramic particles do not exhibit any clear trend on either increasing or decreasing relaxation times in these dynamic processes, compared with the particle-free PEO. The
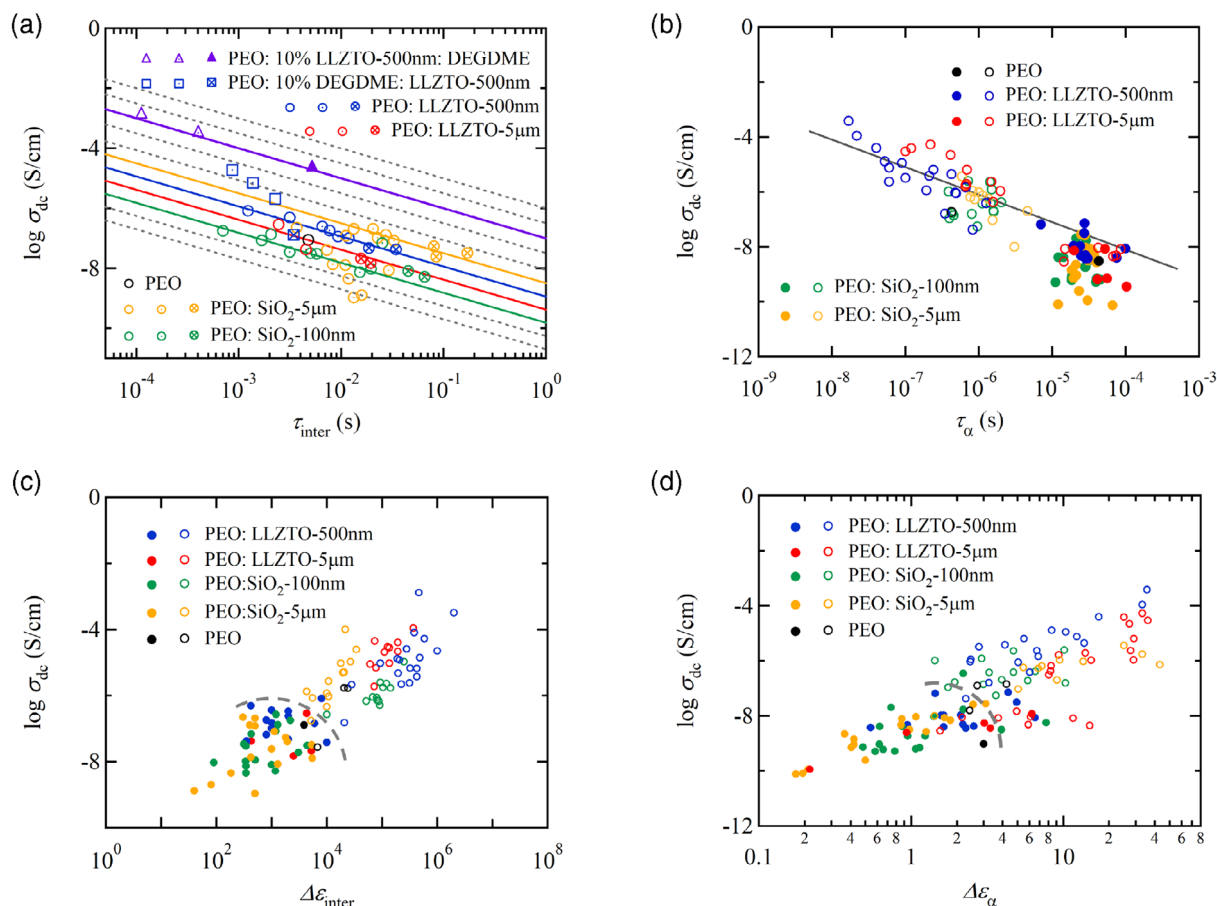
FIGURE 3 DC conductivity versus dynamic process parameters. (a,c) Maxwell–Wagner–Sillars process measured at $T = 30°C$. (b,d) α process measured at $T = 17°C$. All lines in (a,b) demonstrate the same slope of -1, obtained from Equation (3) or Equation (4). Symbols of □, ⊡, and ⊠, together with ◯, ⊙, and ⊗ represent data from samples with increasing weight fraction of LLZTO particles. Symbols of △, ⬚, and ▲ represent data from samples with increasing weight fraction of DEGDME. Closed and open symbols in (b–d) represent samples without and with DEGDME, respectively. Scattering of the same symbols reflects the results from various weight fractions of LLZTO particle and DEGDME plasticizer. The thick dash gray curve roughly indicates the boundary of open and closed data points, that is, with or without DEGDME [Color figure can be viewed at wileyonlinelibrary.com]

results suggest that the strategy of merely adding ceramic particles in PCEs has limited potential to substantially increase ionic conductivity.

Figure 3c,d present similar alterations after DEGDME addition. Promoted $\Delta\varepsilon$ implies a higher concentration of ions participated in transport,[35,36] which further leads to the increase of σ_{dc}. As limited by coordination number, that is, the number of oxygen atoms bonded with Li$^+$,[37] magnitude of $\Delta\varepsilon_\alpha$ increase is far less than that of $\Delta\varepsilon_{inter}$ increase. Nevertheless, the number of sites for α relaxation taking place is expected to be much greater.

2.3 | Mechanism for σ_{dc} improvement

We further analyze the microscopic origins for the σ_{dc} enhancement. The Li$^+$ conductivity can be expressed by:

$$\sigma_{dc} = p\mu q, \tag{5}$$

where p is the concertation of mobile Li$^+$, μ is the Li$^+$ mobility, and q is the elementary charge. The Debye length, a measure of space charge layer thickness at interfaces, can be related to p and q by[38]:

$$L_D = \left(\frac{\varepsilon_s\varepsilon_0 k_B T}{q^2 p}\right)^{1/2}, \tag{6}$$

where k_B is the Boltzmann constant, and T is the absolute temperature. From Equations (1), (2), (5), and (6), p, μ and L_D are determined by:

$$L_D = \left(\frac{\varepsilon_s\varepsilon_0 k_B T}{q^2 p}\right)^{1/2}, \tag{7}$$

$$p = \frac{\varepsilon_s \varepsilon_0 k_B T}{q^2 L_D^2}, \qquad (8)$$

$$\mu = \frac{\sigma_{dc}}{pq}, \qquad (9)$$

and their effects on σ_{dc} are illustrated in Figure 4. These plots show consistent trends of σ_{dc} upon p, μ and L_D in all cases with and without DEGDME, suggesting a strategy for altering σ_{dc}. DEGDME markedly promotes σ_{dc} by increasing concentration of mobile Li^+ (Figure 4a) and reducing L_D at interfaces (Figure 4c), while Li^+ mobility, a measure of ion's ability to move through the PCE, mainly remains at the same level (Figure 4b). Ceramic particle-reinforced PCEs manifest higher p values, with or without the presence of plasticizer, compared with PCEs filled by inert particles. Importantly, the plasticizer reduces activation energy (Figure 2a), releases a portion of inactive Li^+s to participate in ion transport, and thus apparently increases p, as illustrated in Figure 4a. Note

that the dependence rates of σ_{dc} in Figure 4a,c in PCEs with DEGDME are roughly twofold of those in DEGDME-free samples, reflecting effects by accelerated dynamic processes. Combining experimental results above, increasing the density of active ions and simultaneously speeding up micro-dynamic processes for ion movement is an effective strategy for improving σ_{dc}.

From the results in Figures 3 and 4, the effect of particle size on ionic transport is not notably recognized, whereas LLZTO particles demonstrate slightly better electrochemical performance than SiO_2, both well dispersed in PEO.

2.4 | Coupling between relaxation processes

The MWS, α and α_2 processes show a similar dependence upon σ_{dc} with addition of small molecules. This inspires us to explore the interrelation between them. In thermorheologically simple materials, it is assumed that these
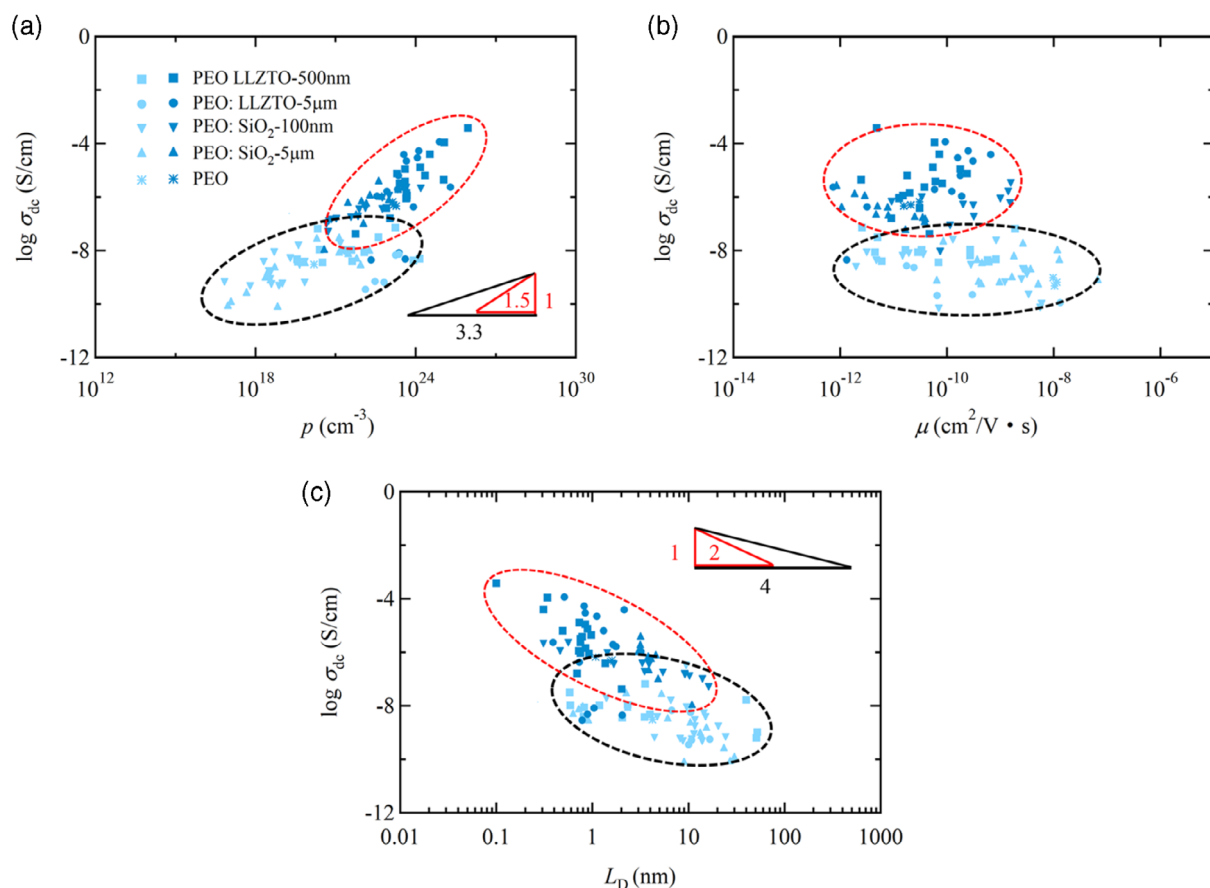

FIGURE 4 Conductivity dependence, on (a) ion concentration, (b) ion mobility, and (c) Debye length, at $T = 17°C$. Black elliptical circles provide guides for the eye, on the range and trend of data from samples without plasticizer addition, whereas the red ellipses show the results from samples with plasticizer. Scattering of the same symbol reflects the results from various weight fractions of particles and DEGDME. The color ramps indicate relative rates in the dependence [Color figure can be viewed at wileyonlinelibrary.com]
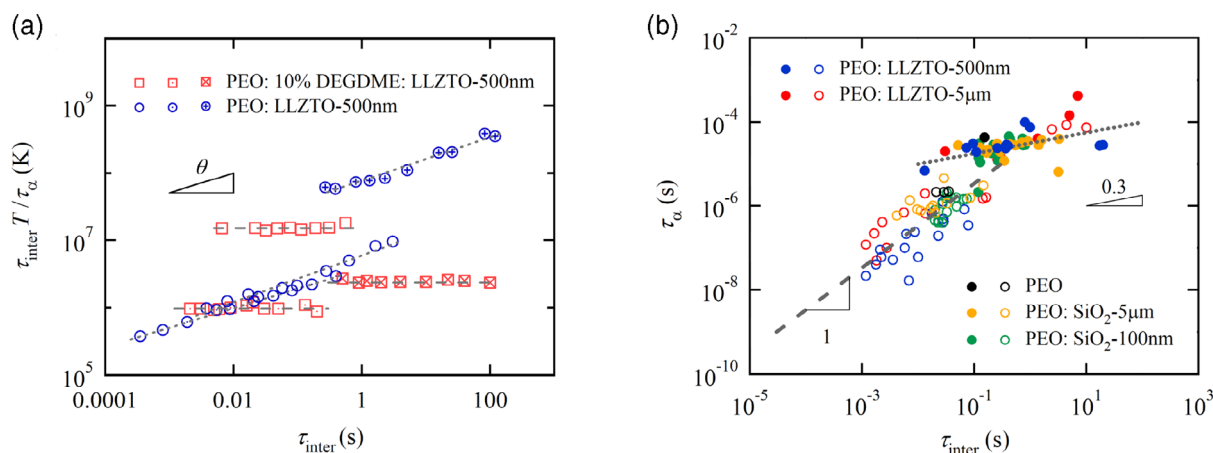
FIGURE 5 Coupling between α relaxation and MWS polarization. (a) $\tau_{inter}T/\tau_\alpha$ and (b) τ_α versus τ_{inter}. The closed and open circles represent samples without and with DEGDME. Symbols of $\square$, $\boxdot$, and $\boxtimes$; $\bigcirc$, $\odot$ and $\otimes$ represent data from samples with increasing weight fraction of LLZTO particles. The decoupling degree θ in (a) for poly(ethylene oxide): LLZTO-500 nm is 0.3. Each data point in (a) represents the result from a single temperature. All data in (b) are measured at 17°C [Color figure can be viewed at wileyonlinelibrary.com]

sub-molecular relaxations manifest an identical temperature dependence, that is, a change in temperature equally shifts the frequency of such relaxations to the same degree. However, this coupling manner does not work under some circumstances. For example, decoupling of chain relaxation from sub-molecular relaxation is detected and attributed to spatial heterogeneity which modifies local structural relaxation.[39] To analyze dynamic processes in PCEs, we adopt a decoupling degree, θ, as an exponent in the equation $\tau_{inter}T/\tau_\alpha = \tau_{inter}^\theta$, which is utilized to evaluate coupling between MWS and α processes. From results in Figure 4, evidently $\tau_{inter}T/\tau_\alpha$ versus τ_{inter} results in a straight line in a double-logarithmic space, as all these variables display a linear dependence to σ_{dc} on a logarithmic scale. Figure 5a depicts coupling relations of representative samples, at various temperatures for each. With the addition of DEGDME, $\tau_{inter}T/\tau_\alpha$ exhibits a horizontal line ($\theta = 0$) that indicates a strong coupling between interfacial dynamics and segmental relaxations in our temperature range. The neat PCE sample shows a linear dependence with a slope $\theta = 0.3$, suggesting a less coupling under such circumstances. Figure 5b directly illustrates correlations between τ_{inter} and τ_α for a family of samples at 17°C. Clearly, adding small molecules makes τ_α be proportional to τ_{inter}, whereas τ_α is proportional to $\tau_{inter}^{0.3}$ for plasticizer-free PCEs, in agreement with the results in Figure 5a. Therefore, the enhanced coupling between τ_{inter} and τ_α, together with a substantial shortening of these relaxation times, that rationalizes both α (including α_2, Figure S22) and MWS dynamics, are concurrently trigged and work in speeding up segmental and ionic motions on a microscopic scale.

It is also worth noting that our results are in line with existing findings or consensuses in the literature. For instance, one of the effects of introducing ceramic particles is widely recognized as to suppress the crystallization of PEO, because amorphous phases majorly contribute to ionic conductivity.[2] Similar endeavors aiming to attain high-level ion dissociations have been made using block copolymers, wherein the short-chain PEO phases are dynamically active due to confinement by adjacent rigid phases from the other block. We found the crystallinities of PEO in our PCE samples remain at a narrow interval (Tables S3 and S4, Figure S11), lower than the particle-free case, even though the weight loading of LLZTO varies in a broad range.[40] Moreover, we noted that the σ_{dc} in our samples varies in a manner quantitatively matching the percolation theory (Figure S10). Our results do not exhibit a clear trend of σ_{dc} change due to the particle size effect, yet it is reported that decreasing nanoparticle size diminishes interfacial effects in polymer-nanoparticle composites.[41]

3 | CONCLUSIONS

In this paper, we demonstrated how dynamic processes quantatively determine ionic conductivity in solid PCEs, and elucidated the mechanism of improving ion transport, which shows that accelerated polymer sub-chain dynamics, together with decreased charge-concentrated interfacial layer which releases more mobile ions, thus dedicates to σ_{dc} enhancement. The findings unveil principles of ion transport in multiphase composites, and offer valuable strategies for increasing σ_{dc} with an emphasis on speeding

up segmental motion and interfacial polarization. It has been recently shown that establishing continuous interfaces along aligned ceramic nanowires effectively increases σ_{dc}.[16–18] The work further confirmed that the increase is originated from the interfacial ion pathways.

In summary, the ion transport mechanism revealed in this work may provide novel approaches for further improvement of ionic conductivity of solid PCEs at ambient temperature, besides keeping their merits ranging from thermal safety, solid yet flexible mechanical properties, and ease for commercial productions.

4 | MATERIAL AND METHODS

4.1 | Materials and sample fabrication

PEO was purchased from Sigma-Aldrich and was used without any further purification. The weight-average molecular weight of the PEO ($M_{W,PEO}$) is 600,000 g/mol. LLZTO particles with average diameters of 5 μm and 500 nm were purchased from Shanghai Kejing Precision Manufacturing. SiO$_2$ particles with diameter of 5 μm and 100 nm were purchased from Shanghai Aladdin Biochemical Technology. Different particle sizes were chosen to influence the pathway forming on polymer/particle interfaces. Fabrication procedure of the polymer-ceramic particle composite electrolytes composed of PEO$_{18}$-LiClO$_{4-x}$ wt% LLZTO or SiO$_2$ is described previously.[40] Briefly, the PCE films were fabricated by blade coating and were subsequently dried by annealing at 50°C under vacuum for 24 h. The thickness of resultant films is around 20–50 μm, depending on different compositions of samples. Distribution and an average size of particles or particle clusters were detected by nano CT imaging (Figures S2–S5 and Table S1). In addition, a certain amount (5, 10, or 20 wt%) DEGMDE (purchased from Macklin Biochemical), was added to the mixture of PEO$_{18}$-LiClO$_4$-5 wt% LLZTO. The nominal weight percentages of LLZTO and SiO$_2$ particles were ascertained by thermogravimetric analysis (Figures S6, S7, Table S2).

4.2 | Dielectric relaxation spectroscopy

DRS measurements were performed by using a Solartron Analyzer. A customized oven with an uncertainty of ± 0.5°C from Shanghai Doaho was equipped for temperature control. The composite electrolytes were measured under an oscillating voltage of 100 mV in the frequency range from 1 MHz to 0.1 Hz at various temperatures. Electrolyte membrane with a diameter of 17 mm and thickness of 20–50 μm was sandwiched between two stainless steel blocking electrodes with a diameter of

16 mm to form a coin cell. The coin cell was firstly heated to an elevated temperature for 10 min to completely melt the PEO crystals, subsequently was quenched to 30°C. The DRS measurements were conducted right after 16 h at T_c to ensure full development of crystallization. The crystallization process was reported in our previous work.[40] It is worth noting that water absorption has a significant impact. It causes an unusual increase in ionic conductivity and the results were not reproducible after heat treatment. Hence, all of our samples were prepared in an argon glovebox. Measurements were carried right after annealing to avoid long-time storage in the glovebox. Samples after 24 h annealing treatment are proved no residual acetonitrile (2100–2400 cm^{-1}) and absorbed water by fourier transform infrared spectroscopy (FTIR), as shown in Figure S8. We double checked if the samples contained any water after characterizations.

For PEO-based electrolytes, the dielectric response is dominated by charge carriers, that is, the Ohmic conduction preponderates in dielectric spectra. It shows above glass transition temperature as a linear increase with decreasing frequency of the dielectric loss on a logarithmic scale:

$$\varepsilon''_\sigma(\omega) = \frac{\sigma_{dc}}{\omega \varepsilon_0}, \tag{10}$$

where ε_0 is dielectric permittivity of vacuum ($\varepsilon_0 = 8.854 \times 10^{-12}$ V^{-1} m^{-1}). Although it does not cover up the whole frequency range (see details in the Appendix), its contribution is considered a limiting factor as it may obscure loss peaks of dipole origin. Hence this effect should be eliminated to elucidate high-frequency relaxation processes, by using the Kramers–Kronig relationship. The Ohmic-conduction free loss was thus determined from derivative of ε'_r[42,43]:

$$\varepsilon''_{der}(\omega) = -\frac{\pi}{2} \frac{\partial \varepsilon''_r(\omega)}{\partial \ln \omega}. \tag{11}$$

Wübbenhorst and co-workers[43] have shown that this method is a close approximation of the conduction-free loss in highly conductive systems.

Relaxation processes at high frequencies (α and α_2) were then analyzed by the Havriliak–Negami (HN) function[44]:

$$\varepsilon^*_{HN}(\omega) = \varepsilon_\infty + \frac{\Delta \varepsilon}{\left(1 + (i\omega \tau_{HN})^a\right)^b}, \tag{12}$$

where $\varepsilon^*_{HN}(\omega) = \varepsilon'_r(\omega) - i\varepsilon''_r(\omega)$, ω is angular frequency, and a and b are shape parameters satisfying constraints

$0 < a$, and $ab < 1$, $\Delta\varepsilon = \varepsilon_s - \varepsilon_\infty$, ε_s and ε_∞ are the unrelaxed ($\omega = 0$) and relaxed ($\omega = \infty$) values of the dielectric permittivity, respectively. EP process is fitted by Debye model ($a = b = 1$ in Equation (12)).

Similarly, the MWS process at low frequencies was analyzed by an empirical modification of the Macdonald model[45]:

$$\varepsilon_{inter}^*(\omega) = \varepsilon_\infty + \frac{\Delta\varepsilon_{inter}}{(i\omega\tau_{inter})^{1-m} + i\omega\tau_{inter}}, \qquad (13)$$

where the subscript inter indicates the interfacial polarization, and $0 < m < 1$. Equation (13) is mathematically equivalent to a constant phase element-type equivalent circuit. We find it works fairly well in fitting MWS, with m determined to be 0.91–0.99. Note that inappropriate fitting may result in an unlimited increase of both real and imaginary permittivities at low frequencies,[46] since the imaginary part of permittivity is proportional to dissipation energy and vanishes when the real part approaches ε_s.

However, as the shape of the loss curve is very sensitive to the subtraction of dc conductivity,[47,48] loss peaks appear much narrower in ε''_{der} than in ε''_r. Hence the derivative analysis should only be used to extract the relaxation time. The rest parameters ($\Delta\varepsilon$, ε_∞ and shape parameters a, b, m) are refined from the raw data $\varepsilon_r^*(\omega) = \varepsilon'_r(\omega) - i\varepsilon''_r(\omega)$, which are represented by the sum of individual processes:

$$\varepsilon_r^*(\omega) = \varepsilon_\infty + i\frac{\sigma_{dc}}{\omega\varepsilon_0} + \frac{\Delta\varepsilon_{inter}}{(i\omega\tau_{inter})^{1-m} + i\omega\tau_{inter}} \\ + \sum_{EP,\alpha,\alpha_2} \frac{\Delta\varepsilon}{(1 + (i\omega\tau_{HN})^a)^b}. \qquad (14)$$

The relaxation processes are rather narrow and symmetric, that is, a varies from 0.86–0.95 and $b = 1$ in Equation (12) for segmental relaxations, MWS process described by Equation (13) is also close to the Debye model. The fact suggests low possibilities of process submerging one another and thus assures accuracy. Fitting example is shown in Appendix.

ACKNOWLEDGMENTS

AUTHOR CONTRIBUTIONS
Yage Huang: Investigation (lead); methodology (lead); writing – original draft (lead); writing – review and editing (supporting). **Xintong Mei:** Investigation (equal); writing – review and editing (supporting). **Yunlong Guo:** Funding acquisition (lead); investigation (equal); project administration (lead); supervision (lead); writing – review and editing (lead).

DATA AVAILABILITY STATEMENT

ORCID
Yunlong Guo https://orcid.org/0000-0002-4490-2140

REFERENCES
[1] A. Manthiram, X. Yu, S. Wang, *Nat. Rev. Mater.* **2017**, *2*, 16103.

[2] Q. Zhao, S. Stalin, C.-Z. Zhao, L. A. Archer, *Nat. Rev. Mater.* **2020**, *5*, 229.

[3] B. Kumar, L. G. Scanlon, *J. Power Sources* **1994**, *52*, 261.

[4] J. W. Fergus, *J. Power Sources* **2010**, *195*, 4554.

[5] K. Pan, L. Zhang, W. Qian, X. Wu, K. Dong, H. Zhang, S. Zhang, *Adv. Mater.* **2020**, *32*, 2000399.

[6] H. Huo, Y. Chen, J. Luo, X. Yang, X. Guo, X. Sun, *Adv. Energy Mater.* **2019**, *9*, 1804004.

[7] S. Tang, W. Guo, Y. Fu, *Adv. Energy Mater.* **2021**, *11*, 2000802.

[8] L. Chen, Y. Li, S.-P. Li, L.-Z. Fan, C.-W. Nan, J. B. Goodenough, *Nano Energy* **2018**, *46*, 176.

[9] C. W. Nan, L. Fan, Y. Lin, Q. Cai, *Phys. Rev. Lett.* **2003**, *91*, 266104.

[10] S. Srivastava, J. L. Schaefer, Z. Yang, Z. Tu, L. A. Archer, *Adv. Mater.* **2014**, *26*, 201.

[11] D. G. Mackanic, X. Yan, Q. Zhang, N. Matsuhisa, Z. Yu, Y. Jiang, T. Manika, J. Lopez, H. Yan, K. Liu, X. Chen, Y. Cui, Z. Bao, *Nat. Commun.* **2019**, *10*, 5384.

[12] T. Dam, S. S. Jena, D. K. Pradhan, *J. Phys. Chem. C* **2018**, *122*, 4133.

[13] Z. Li, H.-M. Huang, J.-K. Zhu, J.-F. Wu, H. Yang, L. Wei, X. Guo, *Appl. Mater. Interfaces* **2019**, *11*, 784.

[14] H. Yamada, A. J. Bhattacharyya, J. Maier, *Adv. Funct. Mater.* **2006**, *12*, 525.

[15] J. Maier, *Prog. Solid State Chem.* **1995**, *23*, 171.

[16] W. Liu, S. W. Lee, D. Lin, F. Shi, S. Wang, A. D. Sendek, Y. Cui, *Nat. Energy* **2017**, *2*, 17035.

[17] W. Liu, D. Lin, J. Sun, G. Zhou, Y. Cui, *ACS Nano* **2016**, *10*, 11407.

[18] W. Liu, N. Liu, J. Sun, P.-C. Hsu, H.-W. Lee, Y. Cui, *Nano Lett.* **2015**, *15*, 2740.

[19] J. Wan, J. Xie, X. Kong, Z. Liu, K. Liu, F. Shi, A. Pei, H. Chen, W. Chen, J. Chen, X. Zhang, L. Zong, J. Wang, L.-Q. Chen, J. Qin, Y. Cui, *Nat. Nanotechnol.* **2019**, *14*, 705.

[20] R. M. S. Bouchet, R. Meziane, A. Aboulaich, L. Lienafa, J.-P. Bonnet, T. N. T. Phan, D. Bertin, D. Gigmes, D. Devaux, R. Denoyel, M. Armand, *Nat. Mater.* **2013**, *12*, 452.

[21] M. A. Morris, S. H. Sung, P. M. Ketkar, J. A. Dura, R. C. Nieuwendaal, T. H. Epps III., *Macromolecules* **2019**, *52*, 9682.

[22] I. Nakamura, N. P. Balsara, Z. G. Wang, *Phys. Rev. Lett.* **2011**, *107*, 198301.

[23] Q. Lu, Y.-B. He, Q. Yu, B. Li, Y. V. Kaneti, Y. Yao, F. Kang, Q.-H. Yang, *Adv. Mater.* **2017**, *29*, 1604460.

[24] D.-M. Shin, J. E. Bachman, M. K. Taylor, J. Kamcev, J. G. Park, M. E. Ziebel, E. Velasquez, N. N. Narenwattananon, G. K. Sethi, Y. Cui, J. R. Long, *Adv. Mater.* **2020**, *32*, 1905771.

[25] S. Das, A. Ghosh, *J. Phys. Chem. B* **2017**, *121*, 5422.

[26] Z. Tu, M. J. Zachman, S. Choudhury, S. Wei, L. Ma, Y. Yang, L. F. Kourkoutis, L. A. Archer, *Adv. Energy Mater.* **2017**, *7*, 1602367.

[27] J. Paulsdorf, N. Kaskhedikar, M. Burjanadze, S. Obeidi, N. A. Stolwijk, D. Wilmer, H.-D. Wiemhöfer, *Chem. Mater.* **2006**, *18*, 1281.

[28] U. H. Choi, R. H. Colby, *Macromolecules* **2017**, *50*, 5582.

[29] K. Kobayashi, G. Pagot, K. Vezzù, F. Bertasi, V. D. Noto, Y. Tominaga, *Polymer* **2020**, *53*, 149.

[30] D. Brogioli, F. Langer, R. Kun, F. L. Mantia, *ACS Appl. Mater. Interfaces* **2019**, *11*, 11999.

[31] S. Choudhury, R. Mangal, A. Agrawal, L. A. Archer, *Nat. Commun.* **2015**, *6*, 10101.

[32] F. Kremer, A. Schönhals, P. Lunkenheimer, A. Loidl, A. Huwe, S. A. Różański, G. Floudas, J. Mijovic, L. Hartmann, K. Fukao, P. A. M. Steeman, J. V. Turnhout, R. Böhmer, G. Diezemann, R. Richert, T. Pakula, A. Arbe, J. Colmenero, D. Richter, *Broadband dielectric spectroscopy*, 1st ed., Springer-Verlag, Berlin Heidelberg, New York, NY **2003**.

[33] P. Walden, *Phys. Chem.* **1906**, *55*, 249.

[34] B. Lestrieza, A. Maazouza, J. F. Gerarda, H. Sautereaua, G. Boiteuxb, G. Seytreb, D. E. Kranbuehl, *Polymer* **1998**, *39*, 6733.

[35] B. K. Wheatle, J. R. Keith, S. Mogurampelly, N. A. Lynd, V. Ganesan, *ACS Macro Lett.* **2017**, *6*, 1362.

[36] B. K. Wheatle, N. A. Lynd, V. Ganesan, *ACS Macro Lett.* **2018**, *7*, 1149.

[37] D. Das, A. Chandrasekaran, S. Venkatram, R. Ramprasad, *Chem. Mater.* **2018**, *30*, 8804.

[38] D. Fragiadakis, S. Dou, R. H. Colby, J. Runt, *Macromolecules* **2008**, *41*, 5723.

[39] A. P. Sokolov, K. S. Schweizer, *Phys. Rev. Lett.* **2009**, *102*, 248301.

[40] Y. Huang, M. Ma, Y. Guo, *J. Polym. Sci.* **2020**, *58*, 466.

[41] H. Emamy, S. K. Kumar, F. W. Starr, *Phys. Rev. Lett.* **2018**, *121*, 207801.

[42] J. van Turnhout, M. Wübbenhorst, *J. Non-Cryst. Solids* **2002**, *305*, 50.

[43] M. Wübbenhorst, J. van Turnhout, *J Non-Cryst. Solids* **2002**, *305*, 40.

[44] S. Havriliak, S. Negami, *J. Polym. Sci. C* **1966**, *14*, 99.

[45] G. J. Brug, A. L. G. V. D. Eeden, M. Sluters-Rehbach, J. H. Sluyters, *J. Electroanal. Chem.* **1984**, *176*, 275.

[46] T. S. Sarensen, V. Cornpafib, R. Diaz-Calleja, *J. Chem. Soc. Faraday Trans.* **1996**, *92*, 1947.

[47] A. J. MacKinnon, S. D. Jenkins, P. T. MacGrail, R. A. Pethrick, *Polymer* **1993**, *34*, 3252.

[48] A. J. MacKinnon, S. D. Jenkins, P. T. MacGrail, R. A. Pethrick, *Macromolecules* **1992**, *25*, 3492.

SUPPORTING INFORMATION

Additional supporting information may be found in the online version of the article at the publisher's website.